THROUGH DUST AND LIGHT: CONSTRAINING THE DISTANCE TO THE GBHT 4U 1630-47 THROUGH HIGH RESOLUTION MM AND X-RAY OBSERVATIONS

by

AHMED ABDULLAH ABBASI

Submitted to the Graduate School of Engineering and Natural Sciences
in partial fulfilment of
the requirements for the degree of Master of Science

Sabancı University
July 2025

THROUGH DUST AND LIGHT: CONSTRAINING THE DISTANCE TO THE GBHT 4U 1630-47 THROUGH HIGH RESOLUTION MM AND X-RAY OBSERVATIONS

Approved by:

Prof. EMRAH KALEMCI .....
(Thesis Supervisor)

Prof. TOLGA GÜVER .....

Prof. ÜNAL ERTAN .....

Date of Approval: July, 18, 2025

ABSTRACT

THROUGH DUST AND LIGHT: CONSTRAINING THE DISTANCE TO THE GBHT 4U 1630-47 THROUGH HIGH RESOLUTION MM AND X-RAY OBSERVATIONS

AHMED ABDULLAH ABBASI

Physics M.Sc. THESIS, JULY 2025

Thesis Supervisor: PROF. EMRAH KALEMCI

Keywords: blackhole X-ray binary, 4U 1630-47, dust scattering halo, molecular clouds, X-ray astronomy

Accurately determining the distance to Galactic blackhole X-ray binaries is critical for understanding their intrinsic luminosities, accretion physics, and jet properties. However, for sources which are highly obscured by dust, traditional distance estimation methods often fail. In this thesis, we present a novel imaging-based methodology which utilizes high-resolution millimeter observations from the Atacama Pathfinder Experiment *APEX* combined with X-ray data from *Chandra* to constrain the distance to the galactic blackhole transient (GBHT) 4U 1630-47 through the modeling of its dust scattering halo (DSH).

We identify 15 molecular clouds from the ^{12}CO data and generate synthetic DSH images for all possible near/far configurations of these clouds across a grid of candidate source distances and subsequently fit the images both radially and azimuthally. Our analysis favors a source distance of 11.5 kpc, with strong constraints on several molecular clouds. We perform Monte Carlo analysis to quantify uncertainties and find a robust peak in best-fit distances at 11.5 kpc. While 13.6 kpc also yielded good statistical fits, it is ultimately discarded due to observational inconsistencies.

This thesis demonstrates the power of combining high-resolution mm observations with X-ray imaging to resolve kinematic distance ambiguities and constrain the source distance. The methodology developed here builds upon the foundation laid in Kalemci, Maccarone & Tomsick (2018), and is also presented in E. Kalemci (2025).

ÖZET

TOZ VE IŞIK ARACILIĞIYLA: GBHT 4U 1630-47 KAYNAĞININ UZAKLIĞININ YÜKSEK ÇÖZÜNÜRLÜKLÜ MM VE X-IŞINI GÖZLEMLERIYLE SINIRLANDIRILMASI

AHMED ABDULLAH ABBASI

Fizik Yüksek Lisans Tezi, TEMMUZ 2025

Tez Danışmanı: Prof. Dr. EMRAH KALEMCI

Anahtar Kelimeler: kara delik X-ışını ikili sistemleri, 4U 1630-47, toz saçılma halesi, moleküler bulutlar, X-ışını astronomisi

Galaktik karadelik X-ışını ikili sistemlerinin uzaklığının hassas şekilde belirlenmesi, bu kaynakların içsel ışıma gücü, yığılma fiziği ve jet özelliklerinin anlaşılması açısından kritik öneme sahiptir. Ancak, yoğun şekilde tozla örtülmüş kaynaklar için geleneksel uzaklık tahmin yöntemleri çoğu zaman yetersiz kalmaktadır. Bu tezde, Atacama Pathfinder Experiment (APEX) tarafından sağlanan yüksek çözünürlüklü milimetre gözlemleri ile Chandra'dan elde edilen X-ışını verilerini birleştiren ve 4U 1630-47 isimli galaktik kara delik geçici kaynağının toz saçılma halesini (DSH) modelleyerek uzaklığını kısıtlayan yeni bir görüntüleme tabanlı yöntem sunulmaktadır.

12CO gözlemlerinden 15 moleküler bulutu tespit edip ve bu bulutların olası yakın/uzak yerleşimlerine karşılık gelen tüm aday kaynak uzaklıklarını kullanarak sentetik DSH görüntüleri üretiyor, ardından bu görüntüleri hem radyal hem de açısal olarak eşleştiriyoruz. Analizimiz, bazı moleküler bulutlar üzerinde güçlü kısıtlamalarla birlikte, kaynak uzaklığı olarak 11.5 kpc'yi desteklemektedir. Belirsizlikleri nicellendirmek için Monte Carlo analizi gerçekleştiriyor ve en iyi uyumlu uzaklıklarda 11.5 kpc civarında belirgin bir tepe gözlemliyoruz. 13.6 kpc uzaklığı da istatistiksel olarak iyi uyum sağlamış olsa da, gözlemsel tutarsızlıklar nedeniyle elenmiştir. Bu tez, yüksek

çözünürlüklü milimetre gözlemlerinin X-ışını görüntüleme ile birleştirilmesinin, kinematik uzaklık belirsizliklerini gidermede ve kaynak uzaklığını kısıtlamada ne denli etkili olduğunu ortaya koymaktadır. Bu çalışmada geliştirilen yöntem, Kalemci et. al. (2018) tarafından atılan temeller üzerine inşa edilmiştir ve ayrıca E. Kalemci (2025) çalışmasında da sunulmuştur.

ACKNOWLEDGEMENTS

I would like to express my gratitude to my advisor, Prof. Emrah Kalemci, for his patient insight, encouragement, and support throughout this thesis. His guidance was critical in shaping both the direction and depth of this thesis.

To my parents, thank you for your unwavering support and patience, even when my explanation of "why I was still working" began to sound suspiciously like science fiction. Your quiet confidence in me has been the foundation of everything I have accomplished.

To my friends, thank you for reminding me that life exists beyond cosmic dust and MATLAB crashes. Your humor and presence made the long process infinitely more bearable.

Finally, I owe a special thanks to my teammates Efe and Atakan. Your involvement and insights made this project not only smoother, but enjoyable.

TABLE OF CONTENTS

LIST OF TABLES

LIST OF FIGURES

1. INTRODUCTION

Black hole X-ray binaries (BHXRBs) are amongst the most luminous transient phenomena in the sky, spanning orders of magnitude in luminosity range during outbursts and temporarily becoming the brightest X-ray objects in the sky, sometimes exceeding the Eddington limit (Kalemci, Kara & Tomsick, 2022). This makes them ideal laboratories for the study of accretion physics, jet production, and strong gravity. For such studies, robust physical interpretations of their behavior become critically dependent on one key parameter: the distance to the source.

Accurately measuring the distance to the source becomes an essential problem for determining the intrinsic luminosities, studying the accretion dynamics, and placing the sources on empirical relations such as hardness luminosity diagrams. The distance to the source is also crucial in calculating key system parameters, such as jet velocity, inclination angle, and the size of the source (Dunn, Fender, Körding, Belloni & Cabanac, 2010; Kalemci et al., 2022).

In some ultraluminous X-ray sources, there is strong evidence for super-Eddington accretion (Bachetti, Harrison, Walton, Grefenstette, Chakrabarty, Fürst, Barret, Beloborodov, Boggs, Christensen, Craig, Fabian, Hailey, Hornschemeier, Kaspi, Kulkarni, Maccarone, Miller, Rana, Stern, Tendulkar, Tomsick, Webb & Zhang, 2014; Brightman, Bachetti, Earnshaw, Fuerst, Garcia, Grefenstette, Heida, Kara, Madsen, Middleton, Stern, Tombesi & Walton, 2019). Although there is a debate about the exact mechanism, uncertainties in the distance and inclination angle limit definitive conclusions.

A significant proportion of black hole X-ray binaries (BHXRBs) are found in the inner galactic plane, a region heavily obscured by dust and gas. Consequently, the use of traditional distance determination methods relying on optical and infrared observations is hampered. In many cases, the use of spectroscopic or photometric measurements is rendered unfeasible. Even parallax data from missions like Gaia becomes unreliable due to crowding, high extinction and faintness of the source (Arnason, Papei, Barmby, Bahramian & Gorski, 2021). As a result, alternative

approaches have been developed to ascertain the distances to these sources.

An alternate approach, which involves X-ray spectral modeling, uses transitions between hard and soft spectral states- transitions which typically happen at characteristic Eddington fractions- allowing them to be used as potential standard candles. This approach has been employed by Maccarone & Coppi (2003); Vahdat Motlagh, Kalemci & Maccarone (2019). Although useful, this method heavily relies on assumptions about the black hole mass and accretion geometry, and is sensitive to intrinsic source variability.

Radio observations provide a geometrically motivated alternative route, particularly jet parallax measurements, where the apparent motion of relativistic jets is tracked over time, allowing for direct distance determinations without reliance on source luminosity. This method has been applied with success to a handful of sources (e.g., Atri, Miller-Jones, Bahramian, Plotkin, Deller, Jonker, Maccarone, Sivakoff, Soria, Altamirano, Belloni, Fender, Koerding, Maitra, Markoff, Migliari, Russell, Russell, Sarazin, Tetarenko & Tudose, 2020; Miller-Jones, Jonker, Dhawan, Brisken, Rupen, Nelemans & Gallo, 2009). This technique, however, requires high-resolution time-resolved radio imaging and is limited to sources with sufficiently bright and well-aligned jets.

Another method is based on HI absorption spectroscopy and involves analyzing the absorption features in the radio spectrum along the line of sight to the source. This technique provides constraints on the source distance relative to known galactic rotation models (Burridge, Miller-Jones, Bahramian, Prabu, Streeter, Castro Segura, Corral Santana, Knigge, Tremou, Carotenuto, Fender & Saikia, 2025; Chauhan, Miller-Jones, Raja, Allison, Jacob, Anderson, Carotenuto, Corbel, Fender, Hotan, Whiting, Woudt, Koribalski & Mahony, 2021). The results for the aforementioned, however, can be model-dependent and ambiguous in directions with complex velocity structures.

A comparative analysis of these techniques and their effectiveness relative to Gaia-based parallaxes is provided in Arnason et al. (2021). For bright but highly obscured X-ray sources, one powerful method- and the one we investigate in this thesis- is the use of dust scattering halos (DSHs). Dust scattering halos are produced when X-ray photons scatter off interstellar dust grains. By modeling the radial intensity profiles of these halos, it is possible to constrain the source distance to BHXRBs whilst simultaneously studying the dust distribution along the line of sight to the source (Heinz, Burton, Braiding, Brandt, Jonker, Sell, Fender, Nowak & Schulz, 2015; Predehl, Burwitz, Paerels & Trümper, 2000; Thompson & Rothschild, 2009; Trümper & Schönfelder, 1973; Xiang, Lee, Nowak & Wilms, 2011).

In Kalemci et al. (2018), the DSH of the black hole candidate 4U 1630-47 was modelled using *Chandra* and *Swift* observations in conjunction with low-resolution CO surveys to ascertain the molecular cloud distribution and constrain the distance to the source. Two candidate distances were found: 4.9kpc and 11.5kpc, with the far distance being preferred with the assumption that the primary scattering cloud, MC-80 lay at its far kinematic distance. It was noted, however, that the primary uncertainty of this method came from the limited resolution of the CO data, making it difficult to precisely ascertain the shape, order, and contribution of the clouds along the line of sight.

The primary motivation of this thesis is to improve the accuracy of the distance constraints for X-ray sources through a novel imaging-based methodology presented in E. Kalemci (2025). Building upon the precedent set in Kalemci et al. (2018), we utilize high-resolution millimeter observations from *APEX* to ascertain the 3D structure of the molecular clouds along the line of sight to the source and subsequently generate synthetic DSH images for a variety of cloud configurations and source distances. By fitting these synthetic images to the observed *Chandra* observation (Fig. 1.1), the model can be used to simultaneously constrain the source distance as well as resolve ambiguities in the cloud configuration along the line of sight in a physically motivated and data-rich way.

1.1 Dust Scattering Halos

Dust scattering halos (DSHs) are extended structures of X-ray emission surrounding bright sources, caused by small-angle scattering of X-ray photons by interstellar dust grains located along the line of sight to the source. First predicted by Overbeck (1965), DSHs can be used as a probe to study the distribution and composition of interstellar dust along the line of sight, as well as the geometry and variability of X-ray sources.

When X-rays emitted by a source travel through the interstellar medium, a fraction of the photons are scattered by dust grains. The scattering cross-section is strongly dependent on both the scattering angle and the energy E of the scattering photons (Draine, 2003). Due to the scattered photons taking a longer path, they arrive slightly later than the unscattered ones, creating a delayed, angularly dispersed halo around the source.

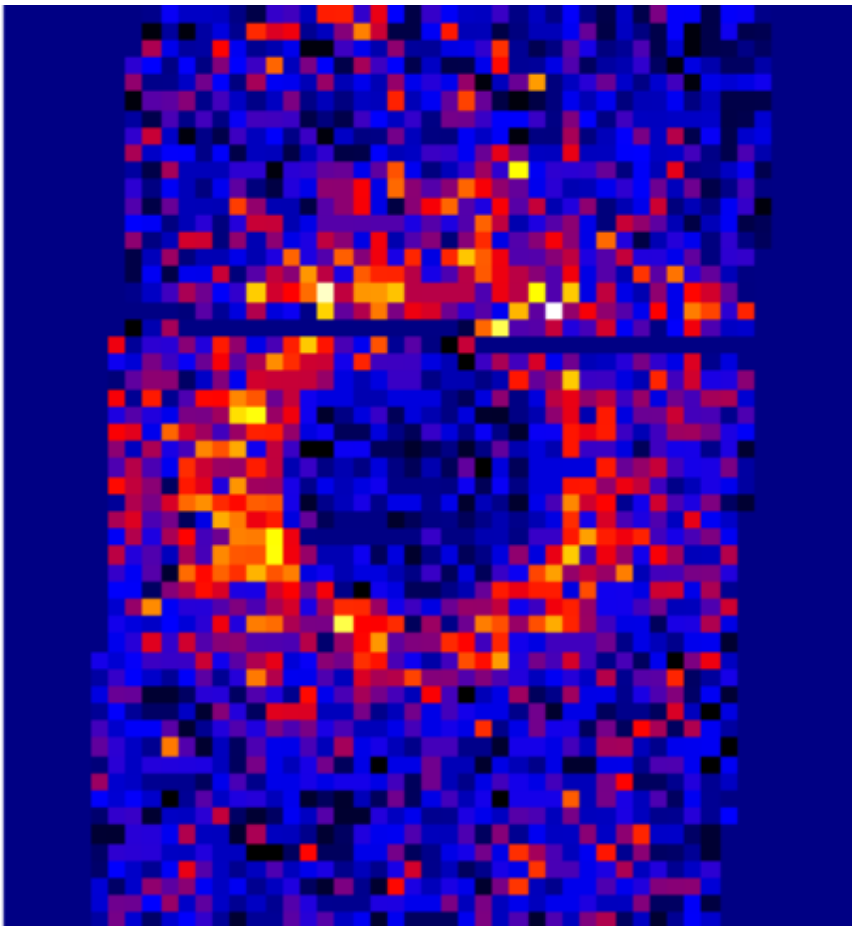

Figure 1.1 *Chandra* observation rebinned to *APEX* resolution

The time delay, Δt, of the scattered photons relative to the unscattered ones after an X-ray flare from a source at distance D, with dust located at a fractional distance xD, can be approximated by the geometric relation:

$$\Delta t \approx \frac{D\,\theta^2}{2c(1-x)}x, \tag{1.1}$$

where c is the speed of light, and θ is the observed angular radius (Predehl & Schmitt, 1995; Trümper & Schönfelder, 1973).

During flares followed by periods of quiescence, dust-scattered emission is observed as one of more diffuse rings moving outwards from the source. These rings (or halos) correspond to the scattering off distinct clouds at different distances along the line of sight, with each ring expanding due to the increasing time delay experienced by scattered photons, providing a direct method to probe both the dust distribution along the line of sight, as well as the distance and geometry of the intervening dust.

The morphology of the halo is strongly dependent on the spatial distribution of the dust. DSHs are observed as uniform rings only if the dust along the line of

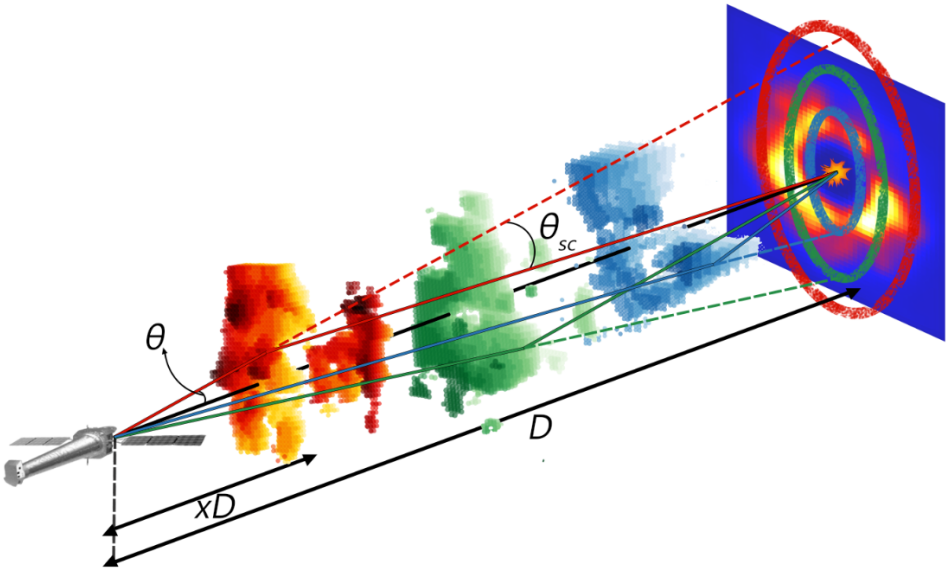

Figure 1.2 Schematic illustration of the dust scattering halo formation using the 3D shapes of molecular clouds. X-rays from the source scatter from interstellar dust located at $x = d_{\rm dust}/d_{\rm src}$, producing a halo observed at angle θ. The distances in the figure are for illustrative purposes and are not fully representative of the actual cloud distances.

sight is uniformly distributed. Realistic clouds, however, often exhibit substantial variations in their column densities, leading to azimuthal inhomogeneities in the scattered emission. As explored in this thesis, the non-uniformity of molecular clouds is encoded in the azimuthal absorption and brightness profile of the DSH.

Beyond their aesthetic appeal, DSHs offer a powerful probe for several astrophysical problems. Some examples of how they have been used are:

- Constraining the distances to X-ray sources through geometric modeling of time-dependent halo profiles (Heinz, Corrales, Smith, Brandt, Jonker, Plotkin & Neilsen, 2016; Xiang et al., 2011).
- Investigating the physical properties and composition of interstellar dust grains (Corrales & Paerels, 2015).
- Measuring the X-ray extinction cross-section and linking it to infrared extinction curves (Corrales, García, Wilms & Baganoff, 2016; Predehl & Schmitt, 1995).
- Studying temporal variations in sources during eclipses or dips by analyzing delayed scattered light (Audley, Nagase, Mitsuda, Angelini & Kelley, 2006).

For a comprehensive recent review, see Costantini & Corrales (2022).

In this study, we investigate both the radial and azimuthal structure of the dust scattering halo of the galactic black hole transient 4U 1630-47. By comparing synthetic halo images generated for all possible cloud configurations for several candidate source distances to the observed *Chandra* observation, we constrain the distance to the source, as well as attempt to resolve ambiguities in the cloud configurations along the line of sight to the source.

1.2 4U 1630-47

The source that is the subject of investigation in this thesis, 4U 1630-47, was first discovered in 1976 with observations with the *Ariel V* satellite (Jones, Forman, Tananbaum & Turner, 1976), and has since been classified as a recurrent X-ray transient system, exhibiting quasi-periodic outburst aprroximately every 2-3 years. Spectral timing analyses of the source suggested the presence of an accreting blackhole, leading to its subsequent classification as a blackhole candidate (Barret, McClintock & Grindlay, 1996). However, its behavior was later noted to not follow the typical hysteresis pattern in the hardness-intensity diagram during state transitions, as reported by Tomsick, Corbel, Goldwurm & Kaaret (2005) and Abe, Fukazawa, Kubota, Kasama & Makishima (2005), thereby prompting further investigation into the nature of the source.

There is further debate regarding the binary classification of 4U 1630-47. Although it is commonly identified as an LMXB, alternative interpretations suggest it may be a Be X-ray binary, given its X-ray variability and spectral features (Kalemci et al., 2018). This ambiguity in classification is underscored by the broader challenges associated with studying the system due to its location and the complex environment along the line of sight.

4U 1630-47 is located in the galactic plane behind a dense and inhomogenous region of the interstellar medium. Observations show that the hydrogen column density ($N_{\rm H}$) towards the source is not only high, but also variable across and within spectral states (Augusteijn, Kuulkers & van Kerkwijk, 2001; Tomsick, Yamaoka, Corbel, Kalemci, Migliari & Kaaret, 2014). This strong and evolving absorption makes constraining the distance to the source using traditional methods especially challenging, thereby introducing significant uncertainties into the interpretation of both its accretion physics and energy output.

Recent measurements of the source's polarization using the *Imaging X-ray Polarimetry Explorer* (*IXPE*) revealed that the source exhibits a high degree of X-ray polarization, indicative of potentially strong scattering or aligned magnetic fields in the inner accretion flow (Krawczynski, Yuan, Chen, Hu, Cavero, Chun, Gau, Steiner & Dovčiak, 2024). The distance to the source is crucial to correctly interpret these measurements, since accurately estimating the distance can improve the reliability of the models describing the observed polarization and the accretion dynamics of the source.

With the limitations of conventional distance indicators for this source, Kalemci et al. (2018) explored the possibility that some of the observed peculiarities of 4U 1630-47 could be attributed to local interstellar dust scattering. By analyzing the DSH observations from *Swift* and *Chandra*, it was demonstrated that detailed modeling of the DSH morphology could provide constraints on the distribution of the intervening dust, as well as the source distance itself, thereby presenting a promising avenue for disentangling source-intrinsic properties from the line of sight effects, particularly in complex regions like that of 4U 1630-47.

1.3 Scientific Motivation and Thesis Goals

The aim of this thesis is to refine the dust scattering halo fitting method first introduced in Kalemci et al. (2018) using high resolution *APEX* ^{12}CO data in conjunction with X-ray data from *Chandra*, *MAXI* and *Swift*, along with 21cm neutral molecular hydrogen emission data from the Southern Galactic Plane Survey (SGPS) in order to constrain the distance to the source 4U 1630-47, and resolve ambiguities in the cloud configurations along the line of sight.

Molecular clouds are typically identified via their CO emission spectra, through which we can ascertain their line-of-sight velocities through Doppler Shifts. These velocities can be converted to distances using Galactic rotation curve models. However, this distance estimate yields two solutions for each radial velocity- a near and a far solution - known as the kinematic distance ambiguity (KDA). Resolving this ambiguity is a fundamental challenge when reconstructing the three dimensional distribution of interstellar material in the galaxy. In our current context, different near/far placements of molecular clouds leads to different halo morphologies. In this work, we simulate all possible DSH images corresponding to near/far configurations

of molecular clouds along the line of sight for several candidate source distances. Each configuration is evaluated by fitting the synthetic images against the observed *Chandra* image using χ^2 minimization.

The thesis is structured as follows:

- Chapter 2 describes the observational datasets used in this work.
- Chapter 3 outlines the simulation pipeline for generating synthetic dust scattering halo images.
- Chapter 4 presents the image fitting results and the best distance estimates for 4U 1630-47.
- Chapter 5 concludes with a discussion of the limitations of the method used and future directions for this work.

2. OBSERVATIONS AND DATA REDUCTION

This work utilizes data from several observatories: we used X-ray data from *Chandra*, *Swift*, and *MAXI*, mm data from *APEX*, as well as publicly available 21cm data from the Southern Galactic Plane Survey (SGPS, (McClure-Griffiths, Dickey, Gaensler, Green, Haverkorn & Strasser, 2005)) to estimate the column density of neutral atomic hydrogen along the line of sight to the source.

2.1 X-ray Data Processing

This work utilizes the X-ray imaging data from *Chandra* ObsID 19004. The data were reduced using standard *Chandra* Interactive Analysis of Observations (CIAO) tools, including background subtraction, point source removal, and rebinning. In this thesis, the resulting cleaned image in the 2.25-3.15 keV energy band is used to extract both radial and azimuthal profiles for fitting with the synthetic DSH images. All image cleaning and processing procedures-including background treatment near chip boundaries and exposure corrections-follow the methodology described in E. Kalemci (2025), which in turn builds on previous work in Kalemci et al. (2018). No additional X-ray image processing was performed as part of this thesis; the final reduced image is instead used as the primary observational input for our halo modelling and fitting analysis.

The X-ray light curve was prepared using a combination of *MAXI* and *Swift* XRT observations, the nuances of which are detailed in E. Kalemci (2025). The light curve provides the time-dependent unabsorbed flux that interacts with intervening molecular clouds and is crucial for modeling the delayed scattered flux observed in the DSH of the source.

Absorbed and unabsorbed fluxes were extracted from *Swift* spectra and fit using

an absorbed disk blackbody model *(tbabs×diskbb)* and cross-calibration scaling factors were obtained by comparing with the *MAXI* fluxes across three energy bands: 1.5–2.25 keV (E1), 2.25–3.15 keV (E2), and 3.15–5 keV (E3).

The light curve preparation was divided into three regions:

- **Region 1** (MJD 57625–57682): Simultaneous *MAXI* and *Swift* observations used to scaling and cross-calibration factors.
- **Region 2** (MJD 57683–57753): Only *MAXI* data were available and were scaled accordingly. This data becomes unreliable beyond MJD 57753, possibly due to the nearby bright source GX 340+0.
- **Region 3** (MJD 57754–57789): An exponential decay model was fitted through available *Swift* observations to interpolate the unabsorbed flux leading up to the *Chandra* observation.

Abrupt spikes and dips in the *MAXI* light curve, which were likely a result of background subtraction and poor exposure, were smoothed. The resulting unabsorbed light curves were subsequently used as input for generating the synthetic DSH surface brightness profiles across each energy band.

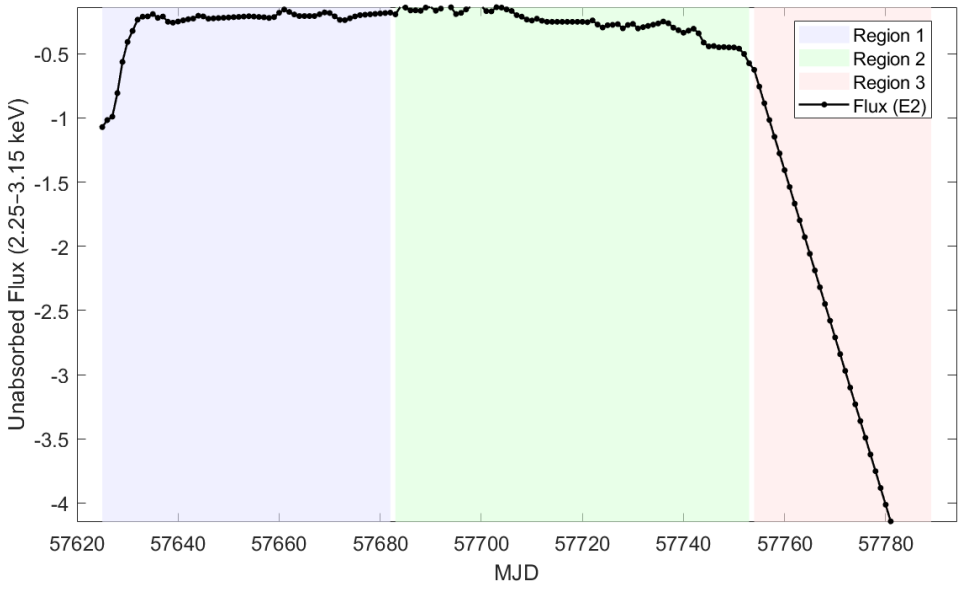

Figure 2.1 Unabsorbed X-ray light curve of 4U 1630–47 in the 2.25–3.15 keV band (E2), combining *Swift* and *MAXI* observations. The shaded regions indicate the time intervals used for cross-calibration (Region 1), interpolation (Region 2), and exponential decay modeling (Region 3).

2.2 APEX CO Data Preparation and Cloud Shape Determination

We utilized molecular line observations of the region surrounding 4U 1630–47 obtained with the 12-meter Atacama Pathfinder Experiment (APEX) telescope. In this work, we mainly use the data for the ^{12}CO and ^{13}CO emission lines for the transition (J = 1-0). The final processed cubes have a spectral resolution of 0.5 km s^{-1} spanning 500 velocity channels from -175 km s^{-1} to $+75$ km s^{-1}, with each pixel corresponding to 13.635".

The 3D molecular cloud structures were determined using the ^{12}CO velocity channel maps along the line of sight to 4U 1630-47. A set of algorithms was developed to determine the 3D representations of the cloud shapes (E. Kalemci, 2025). The ^{12}CO velocity spectrum is decomposed into 15 Gaussian components to identify the peaks in radial velocities and the velocity dispersions of the molecular clouds. The images are subsequently segmented into velocity groups and thresholded to isolate cloud regions. A modified Mean-Shift clustering algorithm, developed by Efe Öztaban (see the appendix in E. Kalemci (2025)), is applied to group data points into distinct clouds and to reconstruct their 3D morphologies. The brightnesses of the pixels are representative of the W(CO), which is later converted into hydrogen column density using the appropriate multiplicative factors. The clouds are named with respect to their peak radial velocities (e.g.,'MC-80'; see Table 3.1).

2.3 SGPS analysis

We used publicly available data from the Southern Galactic Plane Survey (SGPS) to estimate the column density corresponding to neutral atomic hydrogen along the line of sight to 4U 1630-47. The spectral data was decomposed into 11 Gaussians spanning radial velocities from -150 km s^{-1} to 50 km s^{-1} (see Fig.3.2). We found the total column density for the neutral atomic hydrogen along the line of sight to the source by integrating the velocity spectrum as follows (Draine, 2011):

$$N_{H_I} = 1.823 \times 10^{18} \int T_{B,H_I}(v_{LSR}) dv \text{ cm}^{-2} \tag{2.1}$$

This approximation holds under the assumption of optically thin emission-due to self absorption of the H_I 21cm line in denser areas, this provides a lower limit (HI4PI Collaboration, Ben Bekhti, Flöer, Keller, Kerp, Lenz, Winkel, Bailin, Calabretta, Dedes, Ford, Gibson, Haud, Janowiecki, Kalberla, Lockman, McClure-Griffiths, Murphy, Nakanishi, Pisano & Staveley-Smith, 2016). Integrating over the full velocity spectrum via Eqn. 2.1 yields a total neutral atomic hydrogen column density of $2 \times 10^{22}\,\mathrm{cm}^{-2}$, which is in agreement with the lower limit found by Augusteijn, Coe & Groot (2001).

3. MODELING THE DUST SCATTERING HALO

In this section, the simulation pipeline used to generate synthetic images of the DSH of the source 4U 1630-47 is discussed. We vary the source distance between two distance ranges; 4-7 kpc and 10-14 kpc. These ranges were selected based on the analysis presented in Kalemci et al. (2018) where two candidate distances-4.85 kpc and 11.5 kpc- were proposed, with the far distance estimate given the preference. For each trial source distance, we simulate all possible DSH images corresponding to the different cloud configurations (2^{15}). The total neutral atomic hydrogen column density is also varied along the line of sight, enabling simultaneous fitting of both the cloud configuration along the line of sight, as well as the source distance within the same framework.

3.1 Cloud Distances

There are 15 molecular clouds identified along the line of sight using the ^{12}CO spectrum from the *APEX* data. The kinematic distances to the clouds are determined using the A5 model parameters by Reid et al. (2014). Each cloud can be at the near distance or the far distance, depending on which the thickness estimates of the clouds also vary.

The thicknesses of the clouds are determined using the estimates given in Miville-Deschênes, Murray & Lee (2017) for their near and far distances. The parameters for each cloud, including integrated ^{12}CO brightness temperature $W(\mathrm{CO})$, distances from the near and far reaches, and estimated thicknesses, are summarized in Table 3.1.

Table 3.1 Cloud Parameters and Thickness Estimates

No	**Name**	**Near** (kpc)	**Far** (kpc)	**W(CO)**[a] (K km s^{-1})	N_H^b (10^{22} cm^{-2})	Δd_N^c (pc)	Δd_F^c (pc)
1	MC-20	1.82	13.87	3.66	0.15	40	200
2	MC-35	2.71	12.91	1.91	0.08	40	200
3	MC-39	2.92	12.68	4.39	0.18	50	200
4	MC-42	3.07	12.52	1.10	0.04	40	100
5	MC-47	3.31	12.26	1.28	0.05	40	150
6	MC-56	3.72	11.83	1.46	0.06	50	200
7	MC-61	3.93	11.60	1.38	0.06	40	100
8	MC-68	4.21	11.31	6.98	0.28	60	150
9	MC-73	4.40	11.10	7.07	0.28	60	150
10	MC-80	4.67	10.83	29.49	1.18	100	200
11	MC-100	5.38	10.09	2.99	0.12	100	200
12	MC-105	5.55	9.91	2.49	0.10	60	100
13	MC-109	5.69	9.76	1.19	0.05	60	100
14	MC-114	5.87	9.58	0.72	0.03	60	100
15	MC-117	5.98	9.47	0.94	0.04	60	100

[a] Integrated ^{12}CO intensities.

[b] Estimated hydrogen column density using the CO-to-H_2 conversion factor from Bolatto, Wolfire & Leroy (2013).

[c] Estimated cloud thicknesses at near (Δd_N) and far (Δd_F) kinematic distances using the apparent sizes determined by Miville-Deschênes et al. (2017).

3.2 Distance Permutation Generation

There are 15 molecular clouds identified along the line of sight to the source from the peaks in the APEX ^{12}CO velocity spectrum. Each cloud can be placed at either the near distance, or the far distances. The distances are ascertained using the rotation curve from Reid et al. (2014).

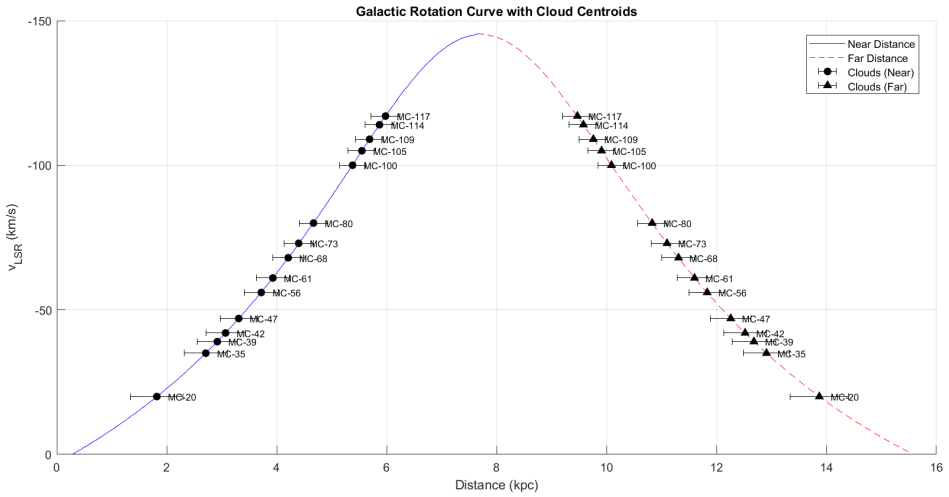

Figure 3.1 Galactic rotation curve adapted from the A5 model of Reid et al. (2014), showing the radial velocity (v_{LSR}) vs. kinematic distance for the direction towards 4U 1630-47. Overlaid markers denote the centroid velocities of molecular clouds identified by the ^{12}CO spectrum, plotted for both near (blue) and far (red) distance solutions, including the uncertainty bars for the model distance errors

For n clouds, there are a total of 2^n possible permutations. A sequential array spanning the distance from the observer to the source is created, and the clouds are added to it based on their near/far distance choice. For some permutations, clouds are placed behind the trial source distance D. Since these do not contribute to the observed halo, clouds placed beyond the source distance are discarded. The sequential array has the same pixel resolution as the APEX data (53×49), with each pixel corresponding to 13.635".

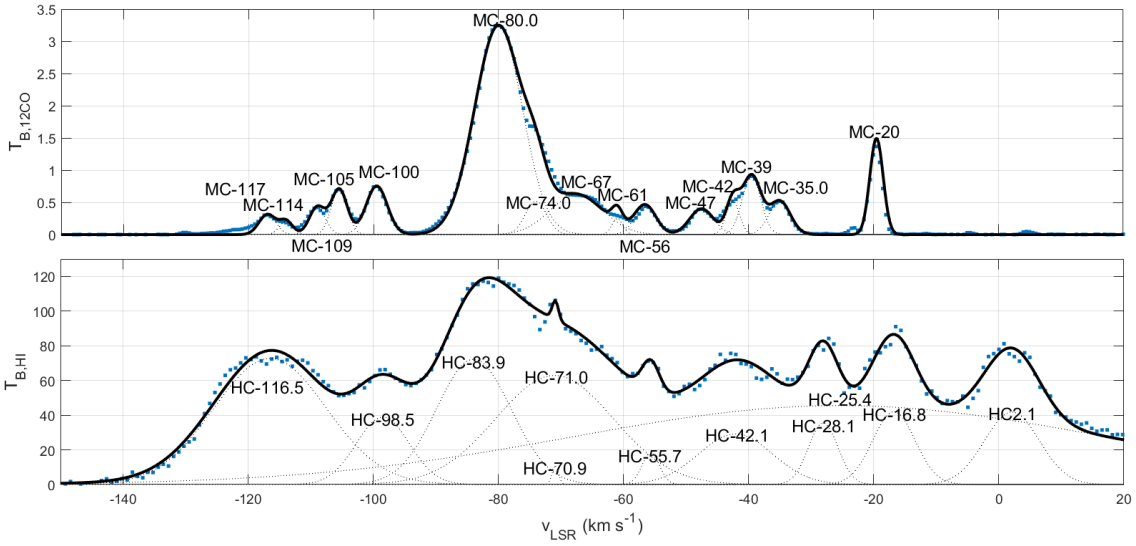

Figure 3.2 Top: ^{12}CO spectrum from *APEX*. Bottom: N_{HI} spectrum from Southern Galactic Plane Survey (*SGPS*)

3.3 Hydrogen Column Density Estimation

The hydrogen column density for each pixel is estimated in three steps:

1.1 **Molecular hydrogen column density ($N_{H_{II}}$)**: The intensity of the ^{12}CO emission for each pixel W(CO) is converted to molecular hydrogen column density via the Bolatto relation (Bolatto et al., 2013):

$$N_{H_{II}} = X_{CO} \times W(CO) \tag{3.1}$$

where $X_{\rm CO} = 2 \times 10^{20}$ cm^{-2} (K km s^{-1})$^{-1}$ (Bolatto et al., 2013).

1.2 **Neutral atomic hydrogen (cloud associated)($N_{H,w}$)**: A fraction of the total neutral atomic hydrogen density is assumed to be associated with the molecular clouds and is added proportional to the molecular hydrogen density of each pixel.

1.3 **Neutral atomic hydrogen (uniformly distributed) ($N_{H,u}$)**: In addition to the neutral atomic hydrogen associated with the molecular clouds, we include a uniform neutral atomic hydrogen density ($N_{H,u}$) from 2.35-12.9 kpc corresponding to the dust in the galactic spiral arms.

The total hydrogen column density for each pixel is therefore:

$$N_H(x_p, y_p) = 2N_{H_{II}}(x_p, y_p) + N_{H,w}(x_p, y_p) + N_{H,u} \tag{3.2}$$

Where (x_p, y_p) denote the x,y position of the scattering pixel in the *APEX* image.

3.4 Extinction Modeling

The next step in the simulation pipeline is modeling the extinction underwent by each photon. This is done in two steps: First, the photon undergoes extinction from the dust and gas along its path from the source to the scattering pixel. Next, it undergoes extinction from the dust and gas from the scattering pixel to the absorber.

The total extinction coefficient can be found for each pixel as:

$$D(x_p, y_p) = \left(\sum_p N_{Hx_p,y_p} + \sum_a N_{Hx_a,y_a} \right) \times \sigma_{ph,E} \tag{3.3}$$

The first sum considers the extinction along the path from the scattering pixel to the observer - the second sum considers the extinction from the clouds along the path from the source to the scattering pixel. Here $\sigma_{ph,e}$ is the photo-electric cross-section for a particular energy band. To ascertain $\sigma_{ph,e}$, we compared the absorbed and unabsorbed fluxes in the Xray spectral fits for each band.

3.5 Time Delay Calculation

For each scattering pixel, we calculate the time delay experienced by a photon scattered at an angle θ relative to the shortest (unscattered) path. The delay is calculated via Eqn. 1.1. Δt determines which portion of the light curve impinges on the flux at each angle.

3.6 Surface Brightness Computation

The surface brightness for each scattering pixel is calculated using:

$$I_\nu(x_p, y_p) = N_{Hx_p,y_p} \frac{d\sigma_{sc,E}}{d\Omega} \frac{F_\nu(t = t_{obs} - \Delta t)}{(1-x)^2} \exp\left[-D(x_p, y_p)\right] \tag{3.4}$$

For every pixel, we find the source flux at the delayed time $F_\nu = (t = t_{obs} - \Delta t)$, and the term $\frac{d\sigma_{\mathrm{sc},E}}{d\Omega}$ is the dust scattering differential cross-section.

The term $\frac{d\sigma_{\mathrm{sc},E}}{d\Omega} \cdot \frac{1}{(1-x)^2}$ is the angular dependence of the scattered intensity and is directly related to the geometry of the scattering setup. This factor is directly computed through the latest version of the *NewDust* code (Corrales, 2023), and is output as the variable `norm_int`, which gives the surface brightness normalized by the incident X-ray flux.

NewDust takes as input a custom grid of scattering angles θ ($0''$ to $600''$ for our

present case) and fractional distances x (ranging from 0.001 to 0.999 with a step size of 0.001). For each combination of x, θ, and photon energy, *NewDust* returns the appropriate normalized surface brightness value.

For this work, we used the Rayleigh-Gans approximation with Drude profile grain absorption (Corrales et al., 2016), and used a dust mass column density $md = 0.000232$ g cm^{-2} per 10^{22} cm^{-2} of hydrogen, corresponding to a dust-to-gas mass ratio of 0.01.

These outputs were generated for three energy bands, each evaluated on the x and θ grid. See section 5.6 for a discussion of *NewDust*.

For each generated image, the World Coordinate System (WCS) information is added and the surface brightness profile is saved as a *FITS* file for further analysis.

3.7 Image Post-Processing and Fitting Methodology

To compare the simulated images with the *Chandra* observation, the image processing and fitting methodology outlined in E. Kalemci (2025) is used. In the aforementioned, the *Chandra* image is cleaned of point sources and rebinned to match the *APEX* resolution, and pixels with low exposure (below 50% of the peak) were masked using the exposure map. The resulting cleaned and rebinned image was then used for all fitting.

Two types of fits were conducted: radial surface brightness profiles, and azimuthal wedge profiles. The radial surface brightness profiles were extracted by summing the photon counts within concentric annuli centered on the source, each with a thickness of 15", and then dividing by the angular area. This procedure was applied to both the observed *Chandra* image and the simulated images. Pixels with low exposure were removed from both the flux summation and the area normalization. For each source distance and cloud configuration, the simulated image was compared to the *Chandra* and the radial profiles were fit via χ^2 minimization. The fit was performed with two free parameters: a multiplicative normalization factor, and a constant background offset.

To take full advantage of the high resolution mm *APEX* data, azimuthal wedge profiles were also generated. The cleaned and rebinned *Chandra* image was divided into radial annuli of width 50", each of which was further subdivided into 18 equal

azimuthal bins (Fig.3.3). The photon flux in each wedge is computed, discounting pixels flagged for low exposure. The signal-to-noise ratio in each wedge is then computed. The resulting wedge profiles for each simulated image were then compared to that of the observed *Chandra* observation. As with the radial fits, a two-parameter χ^2 fit was done with a normalization and a background constant as free parameters. The wedge profiles allow for probing azimuthal features in the DSH, thereby enabling analysis of cloud configurations which yield similar radial profiles, but different azimuthal structures.

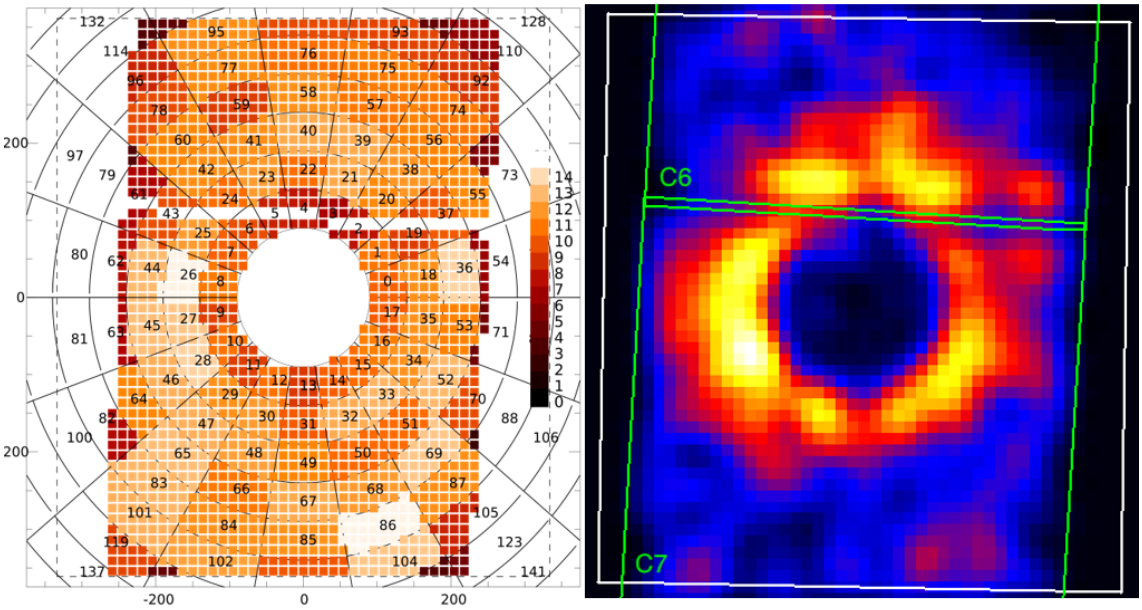

Figure 3.3 **Right:** Cleaned, rebinned, and background-subtracted *Chandra* E2 band image. The *APEX* FOV is shown in the white box. The green box shows the *Chandra* ACIS-s chip boundaries. **Left:** Both *Chandra* and simulated images are divided into the wedge-shaped bins shown. The colors depict the SNR in the *Chandra* E2 image in each wedge.

4. RESULTS

In this chapter, the results of the full image-fitting analysis based on the simulation pipeline presented in the earlier chapter are presented. For each candidate source distance and cloud permutation, synthetic images are generated and compared against the *Chandra* observation and fitted both radially and azimuthally. We use χ^2 minimization to assess goodness of fit. Finally, we analyze errors arising from choice of rotation curve and uncertainties in the light-curve using a Monte-Carlo based approach.

4.1 Radial Fitting Results

To evaluate how well the synthetic images reproduce the observed *Chandra* image, we extracted radial profiles for both the simulated and observed images. Each radial profile was generated by summing fluxes in concentric rings of width 15" and then dividing by the area of the ring. The resulting profiles were fit using a two-parameter model: a normalization factor, and a constant. The goodness of fit was evaluated via χ^2 minimization.

In the 10–14 kpc range, one candidate distance is found as 11.5 kpc with $(N_{H,u}, N_{H,w}) = (2.5 \times 10^{22}, 0)$ cm^{-2}. The reduced χ^2 for the fit is 1.29 with normalization of 0.168 (Fig.4.2). A better fit was found for the 13.6 kpc case with a reduced χ^2 of 1.00 with both $N_{H,u}$ and $N_{H,w}$ as zero (Fig.4.2). The addition of any neutral atomic hydrogen yielded substantially worse fits. A summary of selected best-fit cases is presented in Table 4.1.

In Kalemci et al. (2018), it was suggested that the source could be at the near distance of 4.85 kpc. This estimate yields worse estimates in radial fits compared to 11.5 kpc and 13.6 kpc (see Fig.4.1). The N_H found for 4.85 kpc is also incompatible

Table 4.1 Radial Fit Results

Distance (kpc)	$N_{H,u}$ $10^{22}\,\mathrm{cm}^{-2}$	$N_{H,w}$ $10^{22}\,\mathrm{cm}^{-2}$	χ^2*	**Norm**	**Bkg** ($\mathrm{ph\,cm^{-2}\,s^{-2}\,asec^{-2}}$)	$N_{H,s}$ ($10^{22}\,\mathrm{cm}^{-2}$)
11.5	0	0	2.33	0.72	6.3×10^{-10}	2.43
11.5	1	0	1.77	0.169	4.8×10^{-10}	3.30
11.5	1	2	1.96	0.098	5.4×10^{-10}	4.02
11.5	2.5	0	1.29	0.168	3.3×10^{-10}	4.61
11.5	2.5	2	1.63	0.099	4.6×10^{-10}	6.37
13.6	0	0	1.00	0.767	4.0×10^{-10}	2.43
13.6	1	0	5.91	0.517	-0.3×10^{-11}	3.43
4.85	2	0	2.111	1.048	2.8×10^{-10}	2.51

*Reduced χ^2 with 24 degrees of freedom.

with X-ray observations.

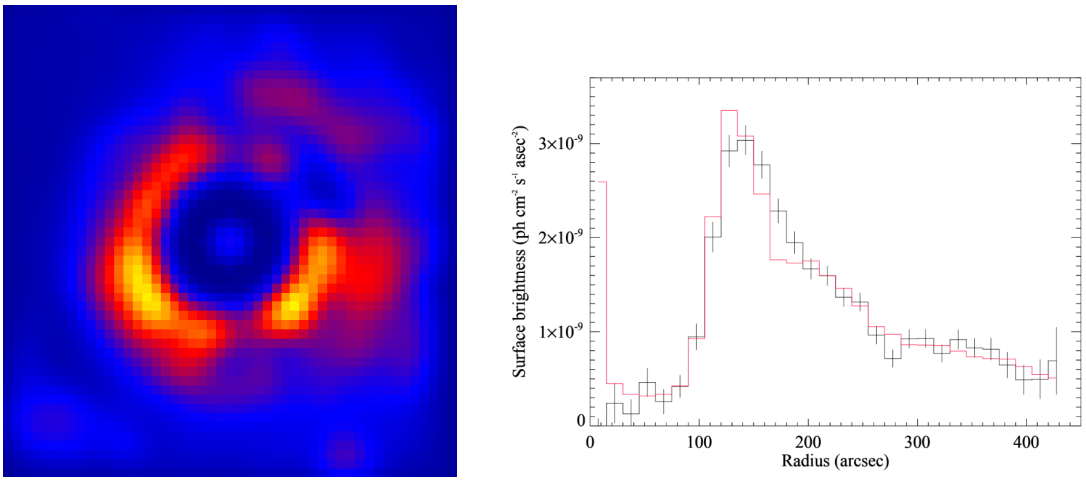

Figure 4.1 The best fit image for 4.85 kpc with $N_{H,u} = 2 \times 10^{22}\mathrm{cm}^{-2}$ and no $N_{H,w}$ with the radial profile on the right.

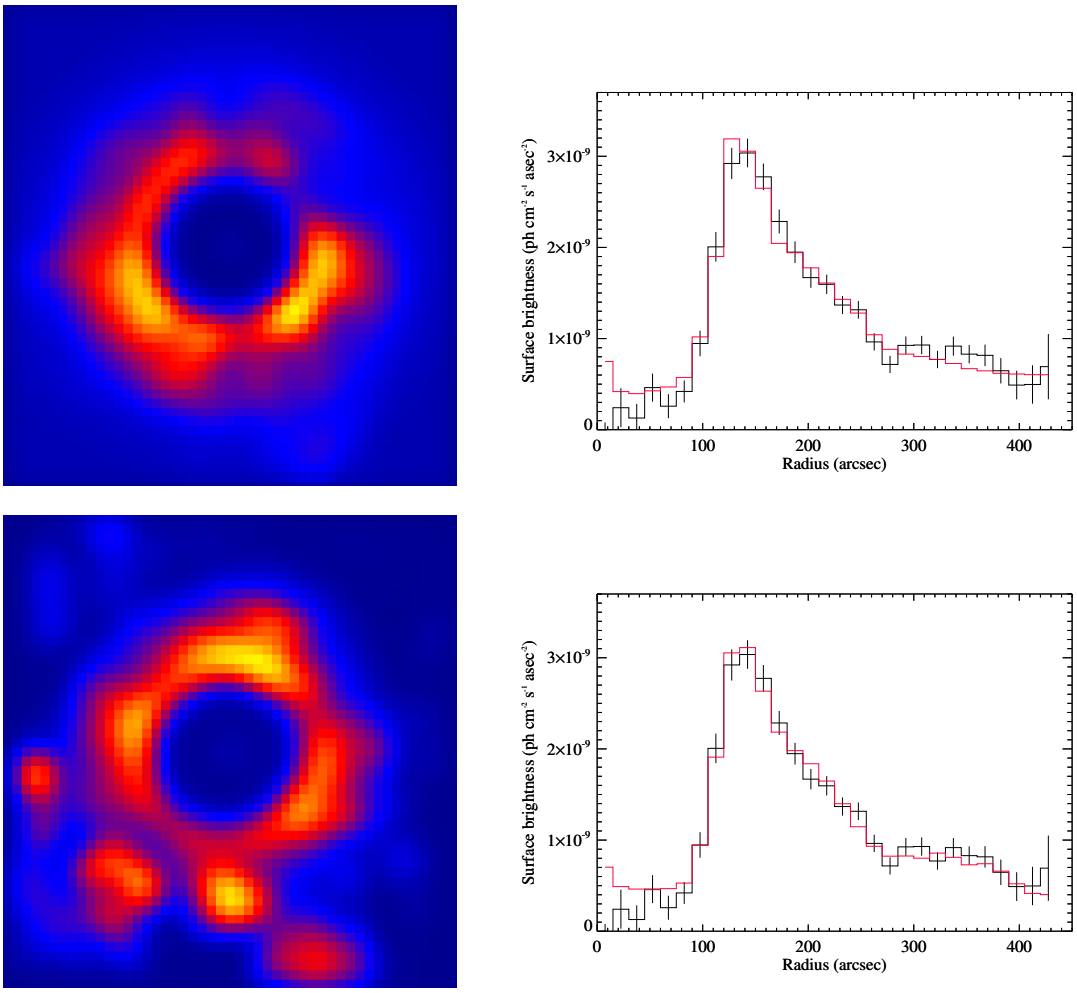

Figure 4.2 Comparison of the best-fit simulated DSH images and corresponding radial surface brightness profiles for two candidate source distances. **Top row:** Fit for 11.5 kpc using $N_{H,u} = 2.5 \times 10^{22}$ cm^{-2} and $N_{H,W} = 0$. **Bottom row:** Fit for 13.6 kpc with no added $N_{H,u}$ or $N_{H,W}$. In both cases, the simulated profiles (solid lines) are fitted to the *Chandra* E2 band data (points with error bars) using χ^2 minimization.

4.2 Azimuthal Fit Results

Azimuthal fitting fully takes advantage of high-resolution millimeter data and 3D cloud shapes by allowing us to analyze specific features arising in the surface brightness profile of the DSH. Wedge profiles were constructed by dividing the field of view into radial annuli, and then further partitioning them into azimuthal sectors and fitting the *Chandra* observation against all the generated simulated images.

The best 11.5 kpc cases yielded reduced χ^2 values between 3.06 and 3.13 for varying $N_{H,u}$ and $N_{H,w}$ values. The 13.6 kpc case once again yielded a lower reduced χ^2 value of 2.02. For the near distance case, placing MC-80 cloud at the near distance yields a best fit distance of 4.85 kpc with a reduced χ^2 of 3.391.

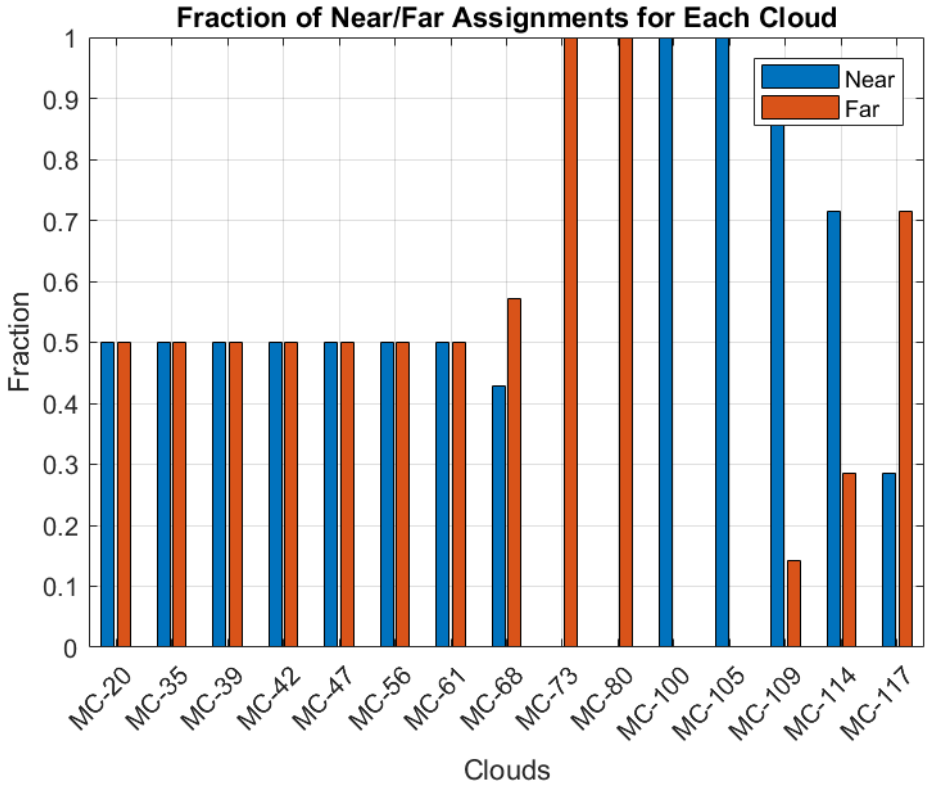

Figure 4.3 Fraction of permutations placing each cloud at the near (blue) or far (red) kinematic distance, computed from the subset of generated images with reduced $\chi^2 < 3.2$ for a source distance of 11.5 kpc. This subset represents approximately 5% of all generated configurations and highlights which cloud placements are most favored by the image-fitting results.

The azimuthal fits allow us to constrain the placement of clouds along the line of sight to the source by studying the individual features each cloud has in the final surface brightness profile of the DSH. Fig.4.3 shows the fractional distribution for all configurations at 11.5 kpc that yielded a reduced $\chi^2 < 3.2$, which corresponds to the $\sim$5% of the azimuthal fits. The analysis indicates that the clouds MC-73, and the main scatterer MC-80 are preferred at the far distance, whereas MC-100 and MC-105 are preferred at the near distance. The clouds MC-109 and MC-114 are predominantly preferred at the near distance, whereas MC-117 is predominantly preferred at the far distance.

Table 4.2 Azimuthal (Wedge) Fit Results

Distance (kpc)	$N_{H,u}$ ($10^{22} cm^{-2}$)	$N_{H,w}$ ($10^{22} cm^{-2}$)	χ^2*	**Norm**	**Bkg** ($\times 10^{-9}$) (ph cm^{-2} s^{-2} asec^{-2})	$N_{H,s}$ ($10^{22} cm^{-2}$)
11.5	0.0	0.0	3.062	0.133	0.90	2.43
11.5	1.0	0.0	3.073	0.131	0.78	3.30
11.5	1.0	1.0	3.065	0.089	0.83	4.02
11.5	1.0	2.0	3.063	0.067	0.85	5.02
11.5	2.0	2.0	3.073	0.067	0.78	5.93
11.5	2.5	0.0	3.128	0.120	0.62	4.61
11.5	2.5	2.0	3.081	0.067	0.75	6.37
13.6	0.0	0.0	2.022	0.736	0.85	2.43
13.6	1.0	0.0	3.446	0.675	-0.3	3.43
4.85	2.0	0.0	3.391	0.732	0.85	2.51

*Reduced χ^2 computed with 67 degrees of freedom. All N_H values are in 10^{22} cm^{-2}. Background (Bkg) is the best-fit constant background level in the azimuthal profile.

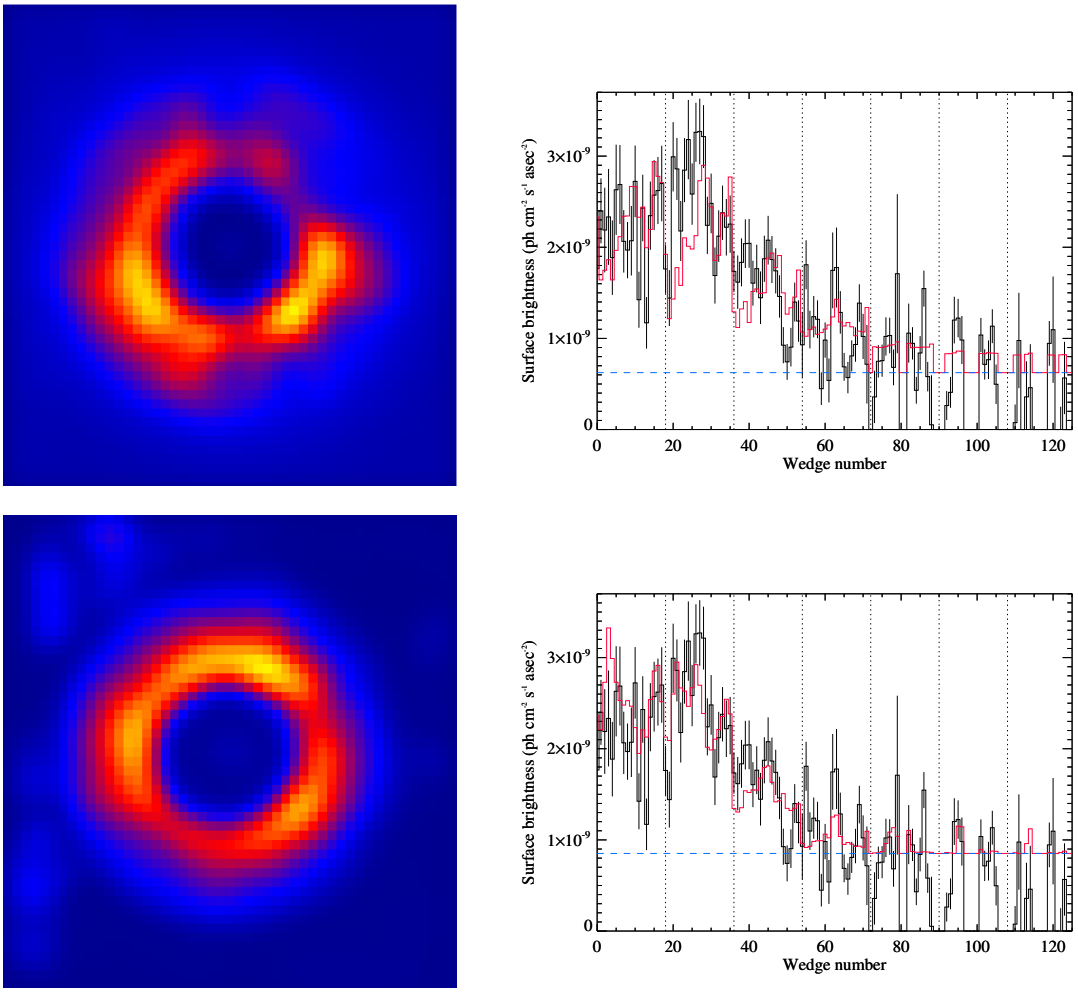

Figure 4.4 Comparison of the best-fit simulated images and corresponding wedge profiles for two candidate source distances. **Top row:** Fit for 11.5 kpc using $N_{H,u} = 2.5 \times 10^{22}$ cm^{-2} and $N_{H,W} = 0$. **Bottom row:** Fit for 13.6 kpc with no added $N_{H,u}$ or $N_{H,W}$. Each wedge profile (right panels) is computed from radial bins divided azimuthally into 18 segments. The vertical dotted lines mark radial bin edges, and the dashed blue line indicates the best-fit background level.

4.3 Uncertainty Arising From Rotation Curve

The reliability of the distance fitting method critically depends on the accurate determination of the distances to the molecular clouds along the line of sight to the source. In other words, the scattering model is highly sensitive to the fractional distance x (Eqn. 3.4) of the clouds to the source. The distances to the clouds are determined based on their line of sight velocities using a galactic rotation curve-in this case, the curve provided by Reid et al. (2014) using the A5 model parameters. The distance estimates to the clouds provided by the curve themselves carry uncertainties that propagate into the final estimate of the source distance. To quantify the impact of these uncertainties, we adopted a marginalization-based, Monte Carlo driven approach.

For the best case cloud configuration found from our radial and azimuthal fits, we treat the distances of each cloud as Gaussian-distributed variables within the uncertainty ranges provided by the rotation curve. For each Monte Carlo iteration, the distances to all the clouds are perturbed with Gaussian noise within their respective uncertainties. Then an image is generated for each perturbed set of cloud distances while varying the source distance by 0.1 kpc between 11.0-12.0 kpc using the simulation pipeline given in the earlier chapters. Each image is then fit to the observed *Chandra* image. For each iteration, a new best-fit distance is recorded. We used 1000 Monte Carlo simulations as a compromise between computational cost and statistical convergence. We verified the key distance estimates and confidence intervals stabilized before this number to ensure the resulting final distribution was sufficiently representative. Each Monte-Carlo realization corresponds to a different set of perturbed cloud distances. We find that the best-fit is consistently found as 11.5 kpc. A histogram of the resulting best-fit distances is shown in Fig.4.5 with 68% and 95% credible regions identified.

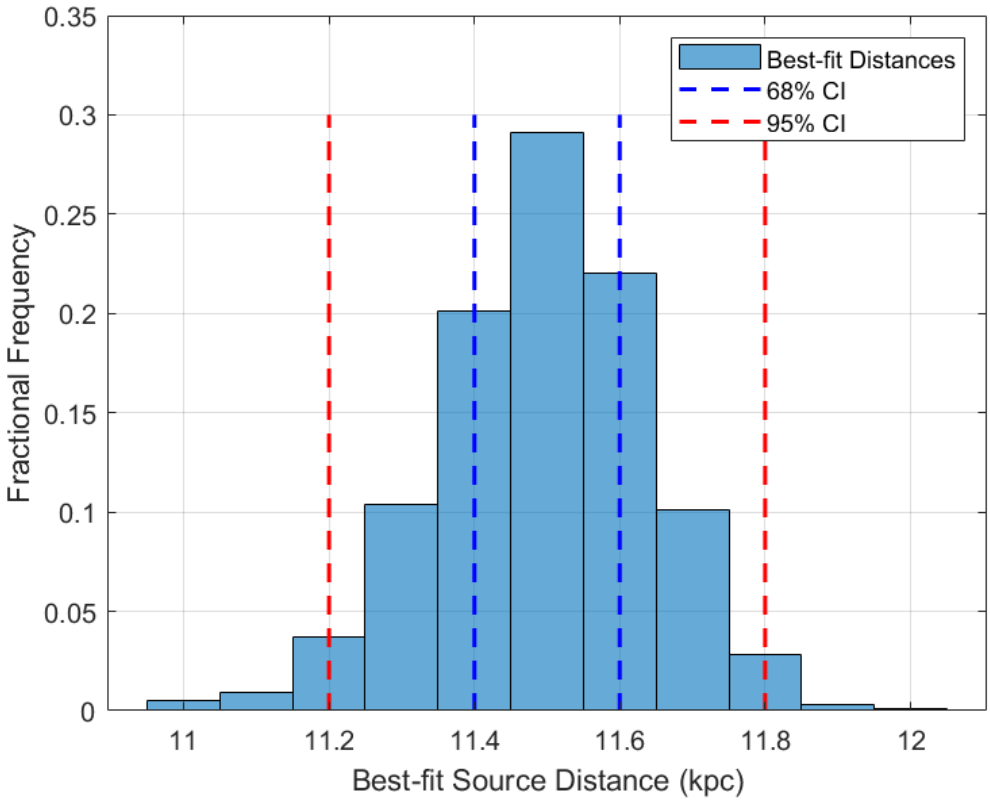

Figure 4.5 Distribution of best-fit source distances obtained from 1000 Monte Carlo iterations where the cloud distances were perturbed within their kinematic uncertainties. The y-axis represents the fractional frequency. The vertical blue dashed lines mark the 68% credible interval, and the red dashed lines indicate the 95% credible interval.

5. CONCLUSIONS AND FUTURE WORK

The methodology outlined in this thesis uses high resolution mm data from *APEX* in conjunction with X-ray observations to simulate synthetic DSH images. There is a set of underlying assumptions and limitations from the observing instruments which affects our results and their interpretation. In this section, we will discuss the key findings in this thesis, our main conclusions, and our treatment of uncertainties and how it affects our final claim.

5.1 Is the source at 4.85 kpc?

In Kalemci et al. (2018), a near distance of 4.85 kpc was proposed as one of the possible distances for 4U 1630-47. 4.85 kpc gets substantially worse radial and azimuthal fits as compared to 13.6 kpc and 11.5 kpc. The best-fit χ^2 values in both cases are poorer, indicating the morphology of the observed DSH is not well modeled under this distance assumption.

The high-resolution *APEX* maps indicate the presence of the clouds MC-100 and MC-105 along the line of sight, both of which have near and far kinematic distances greater than 4.85 kpc. For the near distance case to be viable, these clouds would have to lie behind the source, which would exclude them from contributing to the observed DSH.

In Kalemci et al. (2018), uniform N_H was distributed between fractional distances $x = 0.1$ and $x = 0.99$, even in the near distance case, which condenses a significant amount of dust less than 4.85 kpc from the solar system and not in the spiral arms. In this work, we distribute the uniform N_H between 2.35 kpc and 12.9 kpc, which roughly corresponds to the start and end of the spiral arms in the direction of the source, thereby including the spiral arms along the line of sight. Finally the implied

N_H for the 4.85 kpc case is significantly lower than the values inferred from the X-ray spectral fits. This estimate is also strongly ruled out by Krawczynski et al. (2024) through their analysis of X-ray polarization data from *IXPE*.

With all the aforementioned considerations, in this thesis and in E. Kalemci (2025), we are able to strongly rule out 4.85 kpc as a viable distance for 4U 1630-47.

5.2 The Case of the Missing Ring: Is the source at 13.6 kpc?

The results for both the radial and azimuthal fitting yielded lower reduced χ^2 values for the 13.6 kpc case compared to the other candidate distances. Closer analysis of the simulated and observed DSH morphology, however, reveals critical inconsistencies that argue against this being the source distance.

One issue with 13.6 kpc as the source distance arises from the expected contribution of MC-80- the brightest molecular cloud along the line of sight. If the source is placed at 13.6 kpc and MC-80 is placed at its far distance, the scattering geometry predicts a prominent second ring at angular distances between 200" and 400". This ring should be clearly visible in the *Chandra* observation, but is not (Fig. 5.1). Simulated images with similar configurations show this ring with a brightness comparable to, or even exceeding, that of the primary ring.

Placing MC-80 at the near distance (as is the case in the best fit simulated images for 13.6 kpc) gives rise to other discrepancies. From the Bronfman Survey (Bronfman, Alvarez, Cohen & Thaddeus, 1989), it is observed that MC-80 covers a much larger area than that encompassed by the *APEX* field of view. This alludes to the existence of a second ring, which should have been observed in the *Chandra* image between 600" and 750". Under the assumption of a similar and uniform *W(CO)* beyond the *APEX* field of view, we generated a synthetic image encompassing the *Chandra* field of view (shown in Fig. 5.2). The outer ring has an average brightness of 2.3×10^{-9} ph cm^{-2} s^{-1}, which is almost the same as the brightness of the ring observed between 100" and 200". Despite the inhomogeneities in the molecular cloud, there is no detectable structure of this second ring in the *Chandra* image.

Finally, the best fit for the 13.6 kpc case yields a very low total N_H of 2.4×10^{22} cm^{-2} (see Table 4.2), which is too low as suggested by the X-ray spectral fits. The primary reason for this is that for the best-fit cloud configuration at this distance,

the primary scatterers are MC-35 and MC-39, both of which have substantially lower N_H than MC-80 (see Table 3.1). Furthermore, adding either $N_{H,u}$ or $N_{H,w}$ makes the fits worse. The insufficient column density, combined with the lack of an observed second ring in the *Chandra* observation point to 13.6 kpc being an unlikely distance for the source.

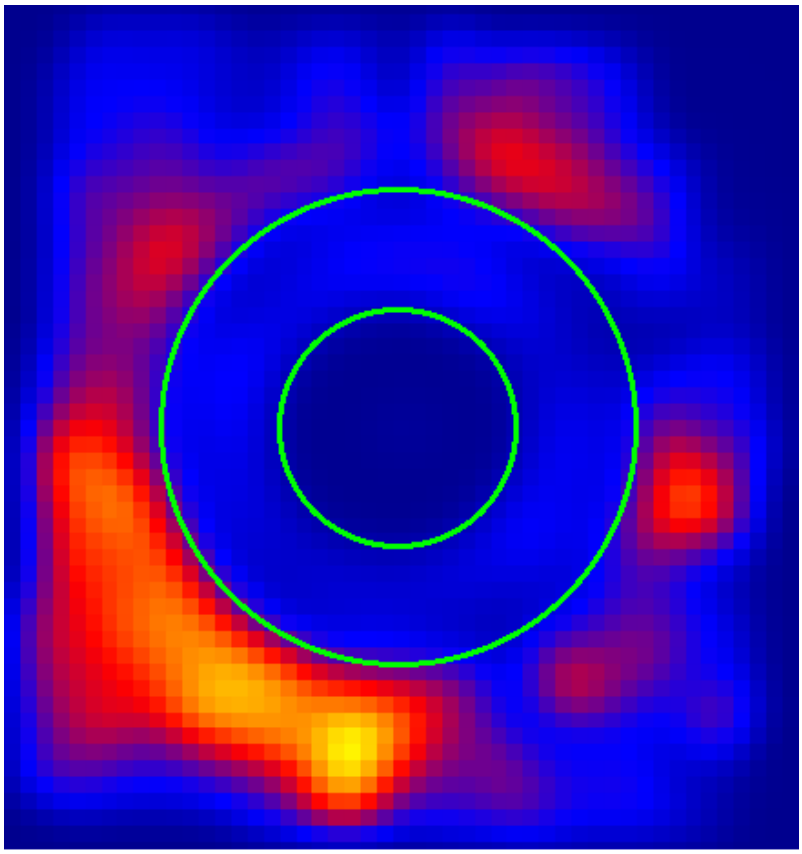

Figure 5.1 Simulated dust scattering halo image with MC-80 placed at its far distance and the source at 13.6 kpc. A prominent outer ring appears at angular distances between 200″ and 400″, arising from scattering off MC-80. The region where the halo is observed in the *Chandra* image is enclosed by the green circles.

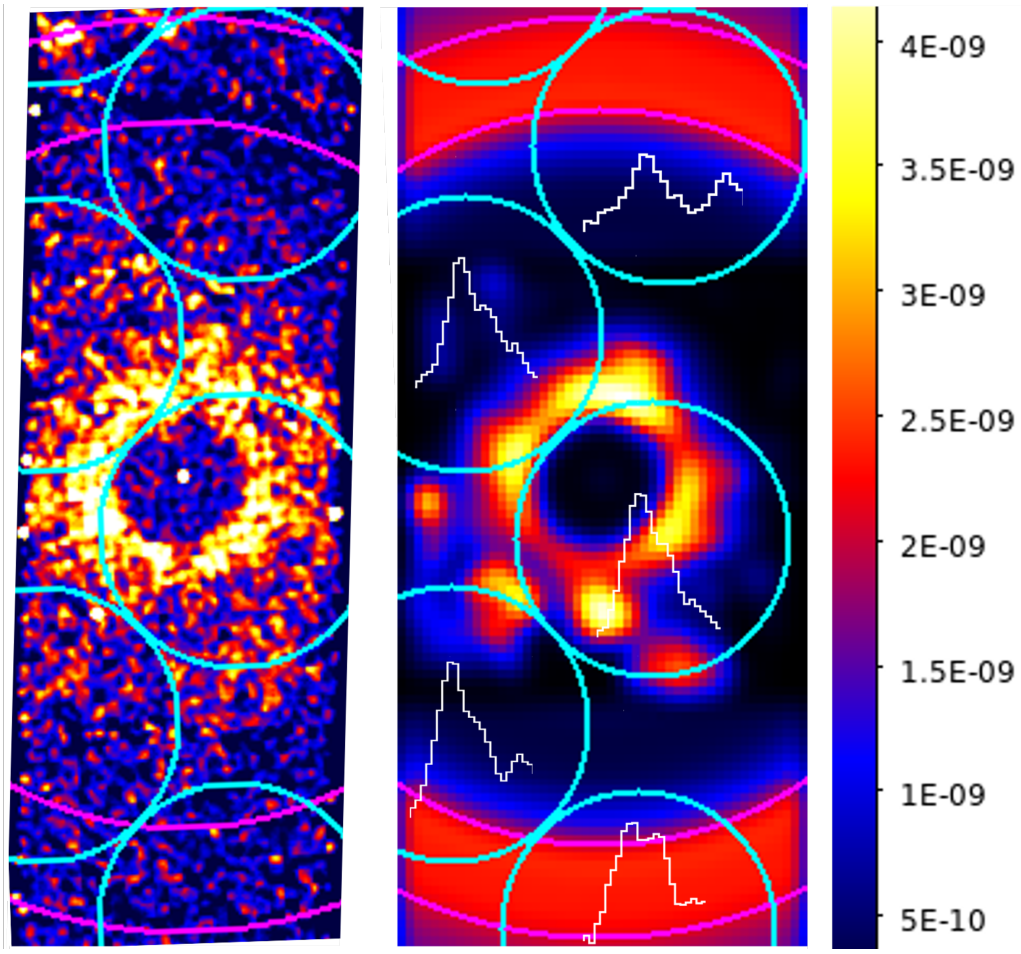

Figure 5.2 **Left:** *Chandra* image with Bronfman survey pointings encircled. **Right:** Best fit image for 13.6 kpc with enlarged field of view with the same regions encircled as the *Chandra* image. The ^{12}CO spectra from the Bronfman survey are shown within the circles. The magenta annuli encompass the region between 600" and 750". The scale is only for the image on the right.

5.3 Uncertainties in Molecular Cloud Distances

One of the key contributors to the uncertainty in our model is the estimation of distances to molecular clouds. Since direct distance measurements are unavailable for most clouds along the line of sight to the source, we rely on kinematic distances inferred from their radial velocities using a rotation curve. This method assumes that clouds move on circular velocities around the galactic center. However, spiral density waves cause non-circular motions, which results in deviations from the assumed circular motion as estimated by the rotation curve (Ramón-Fox & Bonnell, 2017). The radial and azimuthal components of this motion typically result in dispersions less than 10 km s^{-1}, but can be as large as 20 km s^{-1} in some regions close to the galactic center and within the Norma arm (Reid, Menten, Brunthaler, Zheng,

Dame, Xu, Li, Sakai, Wu, Immer, Zhang, Sanna, Moscadelli, Rygl, Bartkiewicz, Hu, Quiroga-Nuñez & van Langevelde, 2019). Therefore, there exists a systematic uncertainty of ~ 0.5 kpc due to the peculiar velocities of the molecular clouds.

Another source of uncertainty in the molecular cloud distance is the choice of the galactic rotation curve. For the sake of consistency with prior work (Kalemci et al., 2018), we used the Reid et al. (2014) rotation curve with the A5 model parameters. The rotation curve itself has uncertainties in its fitted parameters, which propagate to uncertainty in the estimated distance to the molecular clouds, as well as the final source distance. To quantify how the uncertainty within our choice of rotation curve propagates into the final source distance, we implemented a marginalization based Monte Carlo approach (see Section 4.3). The resulting distribution of best-fit distances allowed us to ascertain credible intervals and directly assess the impact of the uncertainty within the rotation curve to our final source distance. The analysis results in robust best-fit peak at 11.5 kpc, in agreement with prior conclusions from Kalemci et al. (2018).

5.4 Resolving ambiguities in KDA

In this thesis and E. Kalemci (2025), as in Kalemci et al. (2018), we ascertained the distances to clouds using the kinematic distance estimation method, which provides two solutions-a near and far solution- for each line of sight velocity, leading to the so called kinematic distance uncertainty (KDA) (Kolpak, Jackson, Bania, Clemens & Dickey, 2003; Schmidt, 1957). Some of the techniques which exist to resolve the KDA include comparing apparent cloud radii with those inferred from molecular linewidths (Solomon, Rivolo, Barrett & Yahil, 1987), using HI absorption features (Riener, Kainulainen, Henshaw & Beuther, 2020), comparison of the apparent radii with the radii estimated from molecular linewidths (Miville-Deschênes et al., 2017), stellar reddening (Schlafly, Green, Finkbeiner, Rix, Bell, Burgett, Chambers, Draper, Hodapp, Kaiser, Magnier, Martin, Metcalfe, Price & Tonry, 2014), associating clouds with spiral arms (Reid, Dame, Menten & Brunthaler, 2016), or the use of trignometric parallaxes through very long baseline interferometry (VLBI) (Reid et al., 2019).

Rather than resolving the KDA with auxiliary methods, in this work, we treat the near/far assignment of each cloud as a free parameter, and allow the radial

and azimuthal fitting methods to determine the most likely configuration based on the statistical goodness-of-fit. This approach allows us to incorporate the full 3D morphology of the clouds ascertained from the high-resolution mm data, relying only on the image fitting to determine which configurations best reproduce the observed DSH.

For our best fit source distance of 11.5 kpc, our method allowed us to constrain 7 out of the 15 molecular clouds based on consistent appearance across the lowest χ^2 fits (see Fig. 4.3). MC-80 and MC-73 are robustly preferred at the far distance, whereas MC-100 and MC-105 are preferred at the near distance, which is in agreement with the findings from Kalemci et al. (2018) and consistent with the linewidth-size relations (Solomon et al., 1987). The clouds which could not be reliably constrained were weak CO emitters, or had a very low fractional distance x, where their contribution to the DSH is diminished due to a low input flux from the source at the time of observation (see Eqn. 1.1). Additional constraints could be placed with sensitive X-ray monitoring of the Halo through the decat phase, which would allow us to pick observations for low x clouds by detecting their scattering observations under brighter illumination.

5.5 Extinction, Absorption and Implications for N_H Modeling

One important source of uncertainty in modeling the dust scattering halo lies in accurately determining the total hydrogen column density along the line of sight. The hydrogen column density affects both the absorbed flux and the scattering intensity (see Eqn. 3.4). In this work, the total hydrogen column density is a sum of three contributions: molecular hydrogen estimated from the ^{12}CO maps using the Bollato conversion factor (Bolatto et al., 2013), a uniform component of neutral atomic hydrogen ($N_{H,u}$), and a cloud-associated component of HI ($N_{H,w}$) distributed proportional to the CO brightness (see Eqn.3.3). This simplified decomposition introduces systematic uncertainties. The Bolatto conversion factor itself has an uncertainty of $\pm$30%. Moreover, the uniform HI distribution used for $N_{H,u}$ likely does not capture complex variation in atomic gas associated with spiral arms or nearby structures. These limitations are further complicated by the uncertainties in the X-ray spectral fits themselves. The N_H obtained through X-ray spectral fits depends strongly on the choice of absorption model, abundances, and cross-sections. For the models used in this work (see Section 2.1), the N_H obtained from the spectral

fits yielded $N_{\rm H} \sim 13 \times 10^{22}{\rm cm}^{-2}$, which is on the high end of the range reported in the literature for 4U 1630-47 ($5–15 \times 10^{22}{\rm cm}^{-2}$, see Díaz Trigo, Migliari, Miller-Jones & Guainazzi (2014);Tomsick et al. (2014);Gatuzz, Díaz Trigo, Miller-Jones & Migliari (2019)). In contrast, the column densities inferred from the molecular and atomic emission in this work reach a maximum of $\sim 6 \times 10^{22}{\rm cm}^{-2}$, nearly a factor of two lower (see Table 4.1; Table 4.2).

Since the input flux is corrected for absorption using a higher N_H than the N_H used for computing the extinction in the scattering, the resulting images are brighter than the observed Chandra image, as seen in the low normalization factors in the case of 11.5 kpc. This discrepancy is compensated for in the fitting process through the normalization factor. For instance, the normalization factor for the best fit 11.5 kpc case is ~ 0.17, indicating the simulated image over-predicts the surface brightness by a factor of $\sim 5-6$. Although the normalization absorbs this mismatch, it might affect the energy-dependent azimuthal distribution, since the extinction by the dust before and after scattering is modeled in two separate phases.

Moreover, the source 4U 1630-47 is known to have a varying column density, despite using the same instrument, abundances, and cross-sections (see E. Kalemci (2025) and references therein), hinting at additional local absorption which is not captured in the N_H derived from emission. This could reduce our mismatch in the normalization factors, and is a possibility backed by other observations (Díaz Trigo et al., 2014; Gatuzz et al., 2019; Kubota, Dotani, Cottam, Kotani, Done, Ueda, Fabian, Yasuda, Takahashi, Fukazawa, Yamaoka, Makishima, Yamada, Kohmura & Angelini, 2007).

Future modeling efforts with the aforementioned in mind could yield more accurate results by incorporating spatially resolved HI absorption maps, allowing for more accurate extinction modeling, or by simultaneously fitting for the dust scattering and absorption in a unified Bayesian framework. Moreover, confirming the presence of local absorption would further reduce our discrepancy in the normalization factors.

5.6 Additional Sources of Uncertainty

Beyond the aforementioned, the methodology in this thesis carries additional sources of uncertainty arising in various phases of modeling the DSH. One source of uncertainty stems from the unreliable part of the lightcurve between MJD 57753 and

57770 (see Section 2.1). A Monte Carlo analysis was performed, assuming an uncertainty of 50% for each data point in the light-curve between the aforementioned dates. For each perturbed light-curve, the synthetic DSH image was generated and the fitting methodology outlined earlier was employed. This yielded in a $\Delta\chi^2 \sim 0.03$. Therefore, the uncertainty in the light-curve results in a negligible variation in the χ^2 values.

Another source of uncertainty stems from choice of dust scattering model used in calculating the scattering cross-sections from *NewDust*. In this thesis, we used the Rayleigh-Gans dust model with Drude approximation. This model assumes a specific dust grain population and composition, as well as a fixed dust-to-gas mass ratio. Moreover, the calculations in *NewDust* are for optically thin media, and may vary for optically thick environments. While *NewDust* provides high-resolution scattering cross-sections, exploring alternative models could quantify how sensitive the results are to our optically thin assumption.

5.7 Final remarks and Future Directions

In this thesis, we developed and implemented a simulation-based framework to model and fit the DSH of the GBHT 4U 1630-47 observed by *Chandra* using high-resolution millimeter data from *APEX*. The primary goal of this work was to build upon the foundation laid in Kalemci et al. (2018) and leverage high-resolution mm data to simultaneously place constraints on the source distance, as well as the placement of clouds along the line of sight to the source by incorporating pixel-resolved cloud morphologies into a custom simulation pipeline. We generated DSH images for all possibilities of near/far distances of the 15 identified molecular clouds across a grid of trial source distances, and fit these images to the observed *Chandra* image using both radial and azimuthal profiles. We identified a best-fit distance and preferred cloud configurations.

Our results favor a distance of 11.5 kpc, consistent with the earlier estimate in Kalemci et al. (2018) whilst discounting both the 4.85 kpc and 13.6 kpc alternatives based on a combination of fitting results, excess halo structure, and inconsistencies in total inferred N_H. Our azimuthal fits enabled us to constrain the placements of 7 out of 15 identified molecular clouds, which are in agreement with predictions from Kalemci et al. (2018) and $\sigma - R$ size-linewidth relations.

We were also able to quantify the uncertainty in our method arising from the choice of rotation curve through a Monte Carlo driven approach, with the resulting posterior distribution confirming the 11.5 kpc estimate within tight confidence bounds. Although prior work explored the azimuthal structure of halos and molecular cloud associations (Heinz et al., 2015), this work represents, to our knowledge, the first implementation of pixel-resolved synthetic DSH image generation using high-resolution mm data for comparison with the observed halo image.

There are several ways to further build upon this work and resolve the limitations in future endeavors. Our analysis shows significant contributions from neutral atomic hydrogen. Extending this modeling approach to include spatially resolved HI maps in the same would refine column density estimates and better recreate the observed halo features.

While we focused on image fitting for a single *Chandra* observation, this framework could be extended to model the time evolution of expanding rings, allowing for time-resolved fitting that could further break degeneracies in scattering geometry and cloud placement. This modeling framework can also be applied to other highly absorbed Galactic X-ray sources with high-resolution CO maps to the same end. With future high-sensitivity and high-resolution X-ray telescopes (e.g. *Lynx*,*AXIS*), the inverse problem-using a known source distance to constrain cloud positions-could be tackled, offering a tool for independently testing Galactic rotation curves.

BIBLIOGRAPHY

Abe, Y., Fukazawa, Y., Kubota, A., Kasama, D., & Makishima, K. (2005). Three Spectral States of the Disk X-Ray Emission of the Black-Hole Candidate 4U 1630- 47. *57*, 629–641.

Arnason, R. M., Papei, H., Barmby, P., Bahramian, A., & Gorski, M. D. (2021). Distances to Galactic X-ray binaries with Gaia DR2. *502*(4), 5455–5470.

Atri, P., Miller-Jones, J. C. A., Bahramian, A., Plotkin, R. M., Deller, A. T., Jonker, P. G., Maccarone, T. J., Sivakoff, G. R., Soria, R., Altamirano, D., Belloni, T., Fender, R., Koerding, E., Maitra, D., Markoff, S., Migliari, S., Russell, D., Russell, T., Sarazin, C. L., Tetarenko, A. J., & Tudose, V. (2020). A radio parallax to the black hole X-ray binary MAXI J1820+070. *493*(1), L81–L86.

Audley, M. D., Nagase, F., Mitsuda, K., Angelini, L., & Kelley, R. L. (2006). ASCA observations of OAO 1657-415 and its dust-scattered X-ray halo. *367*, 1147–1154.

Augusteijn, T., Coe, M., & Groot, P. (2001). XTE J1650-500. *7710*.

Augusteijn, T., Kuulkers, E., & van Kerkwijk, M. H. (2001). The IR counterpart of the black-hole candidate 4U 1630-47. *375*, 447–454.

Bachetti, M., Harrison, F. A., Walton, D. J., Grefenstette, B. W., Chakrabarty, D., Fürst, F., Barret, D., Beloborodov, A., Boggs, S. E., Christensen, F. E., Craig, W. W., Fabian, A. C., Hailey, C. J., Hornschemeier, A., Kaspi, V., Kulkarni, S. R., Maccarone, T., Miller, J. M., Rana, V., Stern, D., Tendulkar, S. P., Tomsick, J., Webb, N. A., & Zhang, W. W. (2014). An ultraluminous X-ray source powered by an accreting neutron star. *514*(7521), 202–204.

Barret, D., McClintock, J. E., & Grindlay, J. E. (1996). Luminosity Differences between Black Holes and Neutron Stars. , *473*, 963.

Bolatto, A. D., Wolfire, M., & Leroy, A. K. (2013). The CO-to-H_2 Conversion Factor. *51*, 207–268.

Brightman, M., Bachetti, M., Earnshaw, H. P., Fuerst, F., Garcia, J., Grefenstette, B., Heida, M., Kara, E., Madsen, K. K., Middleton, M. J., Stern, D., Tombesi, F., & Walton, D. J. (2019). Breaking the limit: Super-Eddington accretion onto black holes and neutron stars. *51*(3), 352.

Bronfman, L., Alvarez, H., Cohen, R. S., & Thaddeus, P. (1989). A deep CO survey of molecular clouds in the southern Milky Way. *71*, 481–548.

Burridge, B. J., Miller-Jones, J. C. A., Bahramian, A., Prabu, S. R., Streeter, R., Castro Segura, N., Corral Santana, J. M., Knigge, C., Tremou, E., Carotenuto, F., Fender, R., & Saikia, P. (2025). On the distance to the black hole X-ray binary Swift J1727.8−1613. *arXiv e-prints*, (pp. arXiv:2502.06448).

Chauhan, J., Miller-Jones, J. C. A., Raja, W., Allison, J. R., Jacob, P. F. L., Anderson, G. E., Carotenuto, F., Corbel, S., Fender, R., Hotan, A., Whiting, M., Woudt, P. A., Koribalski, B., & Mahony, E. (2021). Measuring the distance to the black hole candidate X-ray binary MAXI J1348-630 using H I absorption. *501*(1), L60–L64.

Corrales, L. (2023). eblur/newdust: Python extinction and scattering halo calculations for astrophysical particulates.

Corrales, L. R., García, J., Wilms, J., & Baganoff, F. (2016). The dust-scattering component of X-ray extinction: effects on continuum fitting and high-resolution absorption edge structure. *458*, 1345–1351.

Corrales, L. R. & Paerels, F. (2015). The dust scattering halo of Cygnus X-3. *453*, 1121–1135.

Costantini, E. & Corrales, L. (2022). Interstellar Absorption and Dust Scattering. In C. Bambi & A. Sangangelo (Eds.), *Handbook of X-ray and Gamma-ray Astrophysics* (pp.40̃).

Díaz Trigo, M., Migliari, S., Miller-Jones, J. C. A., & Guainazzi, M. (2014). XMM-Newton observations reveal the disappearance of the wind in 4U 1630-47. *571*, A76.

Draine, B. T. (2003). Scattering by Interstellar Dust Grains. II. X-Rays. , *598*(2), 1026–1037.

Draine, B. T. (2011). *Physics of the Interstellar and Intergalactic Medium*. Princeton: Princeton University Press.

Dunn, R. J. H., Fender, R. P., Körding, E. G., Belloni, T., & Cabanac, C. (2010). A global spectral study of black hole X-ray binaries. , *403*(1), 61–82.

E. Kalemci, M. Díaz Trigo, E. O. A. A. A. T. S. J. A. T. T. J. M. A. S. E. v. N. J. C. A. M. J. B. B. (2025). Dust scattering halo of 4u 1630-47: High resolution x-ray and mm observations constrain source and molecular cloud distances. manuscript submitted.

Gatuzz, E., Díaz Trigo, M., Miller-Jones, J. C. A., & Migliari, S. (2019). Chandra high-resolution spectra of 4U 1630-47: the disappearance of the wind. , *482*(2), 2597–2611.

Heinz, S., Burton, M., Braiding, C., Brandt, W. N., Jonker, P. G., Sell, P., Fender, R. P., Nowak, M. A., & Schulz, N. S. (2015). Lord of the Rings: A Kinematic

Distance to Circinus X-1 from a Giant X-Ray Light Echo. *806*(2), 265.

Heinz, S., Corrales, L., Smith, R., Brandt, W. N., Jonker, P. G., Plotkin, R. M., & Neilsen, J. (2016). A Joint Chandra and Swift View of the 2015 X-ray Dust-scattering Echo of V404 Cygni. *825*, 15.

HI4PI Collaboration, Ben Bekhti, N., Flöer, L., Keller, R., Kerp, J., Lenz, D., Winkel, B., Bailin, J., Calabretta, M. R., Dedes, L., Ford, H. A., Gibson, B. K., Haud, U., Janowiecki, S., Kalberla, P. M. W., Lockman, F. J., McClure-Griffiths, N. M., Murphy, T., Nakanishi, H., Pisano, D. J., & Staveley-Smith, L. (2016). HI4PI: A full-sky H I survey based on EBHIS and GASS. *594*, A116.

Jones, C., Forman, W., Tananbaum, H., & Turner, M. J. L. (1976). Uhuru and Ariel V observations of 3U 1630-47: a recurrent transient X-ray source. *210*, L9–L11.

Kalemci, E., Kara, E., & Tomsick, J. A. (2022). Black Holes: Timing and Spectral Properties and Evolution. In C. Bambi & A. Sangangelo (Eds.), *Handbook of X-ray and Gamma-ray Astrophysics* (pp.9̃).

Kalemci, E., Maccarone, T. J., & Tomsick, J. A. (2018). A Dust-scattering Halo of 4U 1630-47 Observed with Chandra and Swift: New Constraints on the Source Distance. , *859*(2), 88.

Kolpak, M. A., Jackson, J. M., Bania, T. M., Clemens, D. P., & Dickey, J. M. (2003). Resolving the Kinematic Distance Ambiguity toward Galactic H II Regions. *582*(2), 756–769.

Krawczynski, H., Yuan, Y., Chen, A. Y., Hu, K., Cavero, N. R., Chun, S., Gau, E., Steiner, J. F., & Dovčiak, M. (2024). Evaluation of Several Explanations of the Strong X-Ray Polarization of the Black Hole X-Ray Binary 4U 1630-47. *Astrophys. J. Lett.*, *977*(1), L10.

Kubota, A., Dotani, T., Cottam, J., Kotani, T., Done, C., Ueda, Y., Fabian, A. C., Yasuda, T., Takahashi, H., Fukazawa, Y., Yamaoka, K., Makishima, K., Yamada, S., Kohmura, T., & Angelini, L. (2007). Suzaku Discovery of Iron Absorption Lines in Outburst Spectra of the X-Ray Transient 4U 1630-472. *59*, 185–198.

Maccarone, T. J. & Coppi, P. S. (2003). Hysteresis in the light curves of soft X-ray transients. *338*, 189–196.

McClure-Griffiths, N. M., Dickey, J. M., Gaensler, B. M., Green, A. J., Haverkorn, M., & Strasser, S. (2005). The Southern Galactic Plane Survey: H I Observations and Analysis. *158*(2), 178–187.

Miller-Jones, J. C. A., Jonker, P. G., Dhawan, V., Brisken, W., Rupen, M. P., Nelemans, G., & Gallo, E. (2009). The First Accurate Parallax Distance to a Black Hole. , *706*(2), L230–L234.

Miville-Deschênes, M.-A., Murray, N., & Lee, E. J. (2017). Physical Properties of Molecular Clouds for the Entire Milky Way Disk. *834*, 57.

Overbeck, J. W. (1965). Small-Angle Scattering of Celestial X-Rays by Interstellar Grains. *141*, 864.

Predehl, P., Burwitz, V., Paerels, F., & Trümper, J. (2000). Chandra measurement of the geometrical distance to Cyg X-3 using its X-ray scattering halo. *357*, L25–L28.

Predehl, P. & Schmitt, J. H. M. M. (1995). X-raying the interstellar medium: ROSAT observations of dust scattering halos. *293*, 889–905.

Ramón-Fox, F. G. & Bonnell, I. A. (2017). Streaming motions and kinematic distances to molecular clouds. *474*(2), 2028–2038.

Reid, M. J., Dame, T. M., Menten, K. M., & Brunthaler, A. (2016). A Parallax-based Distance Estimator for Spiral Arm Sources. , *823*(2), 77.

Reid, M. J., Menten, K. M., Brunthaler, A., Zheng, X. W., Dame, T. M., Xu, Y., Li, J., Sakai, N., Wu, Y., Immer, K., Zhang, B., Sanna, A., Moscadelli, L., Rygl, K. L. J., Bartkiewicz, A., Hu, B., Quiroga-Nuñez, L. H., & van Langevelde, H. J. (2019). Trigonometric Parallaxes of High-mass Star-forming Regions: Our View of the Milky Way. *885*(2), 131.

Reid, M. J., Menten, K. M., Brunthaler, A., Zheng, X. W., Dame, T. M., Xu, Y., Wu, Y., Zhang, B., Sanna, A., Sato, M., Hachisuka, K., Choi, Y. K., Immer, K., Moscadelli, L., Rygl, K. L. J., & Bartkiewicz, A. (2014). Trigonometric Parallaxes of High Mass Star Forming Regions: The Structure and Kinematics of the Milky Way. *783*, 130.

Riener, M., Kainulainen, J., Henshaw, J. D., & Beuther, H. (2020). Autonomous Gaussian decomposition of the Galactic Ring Survey. II. The Galactic distribution of ^{13}CO. *640*, A72.

Schlafly, E. F., Green, G., Finkbeiner, D. P., Rix, H. W., Bell, E. F., Burgett, W. S., Chambers, K. C., Draper, P. W., Hodapp, K. W., Kaiser, N., Magnier, E. A., Martin, N. F., Metcalfe, N., Price, P. A., & Tonry, J. L. (2014). A Large Catalog of Accurate Distances to Molecular Clouds from PS1 Photometry. *786*(1), 29.

Schmidt, M. (1957). Spiral structure in the inner parts of the Galactic System derived from the hydrogen emission at 21-cm wavelength. *Bulletin of the Astronomical Institutes of the Netherlands*, *13*, 247.

Solomon, P. M., Rivolo, A. R., Barrett, J., & Yahil, A. (1987). Mass, luminosity, and line width relations of Galactic molecular clouds. *319*, 730–741.

Thompson, T. W. J. & Rothschild, R. E. (2009). The X-Ray Halo of Cen X-3. *691*, 1744–1753.

Tomsick, J. A., Corbel, S., Goldwurm, A., & Kaaret, P. (2005). X-Ray Observations

of the Black Hole Transient 4U 1630-47 during 2 Years of X-Ray Activity. *630*, 413–429.

Tomsick, J. A., Yamaoka, K., Corbel, S., Kalemci, E., Migliari, S., & Kaaret, P. (2014). A Delayed Transition to the Hard State for 4U 1630-47 at the End of its 2010 Outburst. *791*, 70.

Trümper, J. & Schönfelder, V. (1973). Distance Determination of Variable X-ray Sources. *25*, 445.

Vahdat Motlagh, A., Kalemci, E., & Maccarone, T. J. (2019). Investigating state transition luminosities of Galactic black hole transients in the outburst decay. *485*(2), 2744–2758.

Xiang, J., Lee, J. C., Nowak, M. A., & Wilms, J. (2011). Using the X-Ray Dust Scattering Halo of Cygnus X-1 to Determine Distance and Dust Distributions. *738*, 78.